Delamination defect identification in CFRP laminates using improved elliptical localization and Lamb wave probabilistic imaging

Yuan Chen[1,2,*], Wenbin Liu[3], Binqiang Huang[3], Guangming Zhang[4], Xiang Wan[2,3], Ming Dong[2,3], Xin Su[3]

1College of Sciences, Xi'an University of Science and Technology, Xi'an, Shaanxi, 710054, China

2Shaanxi Key Laboratory of Mine Electromechanical Equipment Intelligent Detection and Control, Xi'an University of Science and Technology, Xi'an, Shaanxi, 710054, China

3College of Mechanical Engineering, Xi'an University of Science and Technology, Xi'an, Shaanxi,710054, China

4School of Engineering, Liverpool John Moores University, Liverpool, L3 3AF, United Kingdom

** Corresponding author: Yuan Chen Email: chenyuan1030@126.com*

Abstract: Carbon fiber-reinforced polymer (CFRP) is widely used in aerospace and other industrial fields due to its high strength-to-weight ratio, excellent temperature and corrosion resistance. However, manufacturing-induced delamination defects can seriously compromise structural integrity, making nondestructive evaluation (NDE) essential. This paper proposes an improved defect identification method that combines an enhanced elliptical localization algorithm with Lamb wave-based probabilistic imaging for promising delamination identification in CFRP laminates under the tested conditions. First, the dispersion curves of Lamb waves are calculated using the 1D-GLL-SAFE method in SAFEDC software, and S_0/A_0 modal wave velocity radar maps are generated to visualize directional dependence in the anisotropic structure. Finite element models with controlled delamination defects are then established in ABAQUS to simulate Lamb wave propagation and defect interaction. Simulation results show absolute localization errors of 3.91mm and 3.61mm, with relative errors of 1.85% and 2.55%. An experimental setup incorporating ultrasonic excitation and fiber Bragg grating (FBG) sensing is developed to test CFRP specimens with pre-embedded defects. Experimental results demonstrate the method's accuracy, with absolute errors of 2.84mm and 3.82mm, corresponding to relative errors of 1.34% and 2.71%. This study provides a validated, integrated solution for high-precision nondestructive testing (NDT) and localization of delamination defects in CFRP structures through simulations and experiments.

Keywords: CFRP; improved elliptical algorithm; Lamb wave probabilistic imaging; defect localization

1 Introduction

With the rapid development of aerospace technology, there is a growing demand for lightweight and high-strength materials [1]. CFRP, as a typical composite material, has been widely used in aerospace and other fields [2-4]. However, due to the complexity of the manufacturing process, CFRP is susceptible to external influences, which can cause defects such as delamination, porosity and matrix cracking. These defects significantly reduce the performance of the composites and can lead to failure of composite components in service. Therefore, it is essential to carry out quality inspection of composite materials [5, 6].

The presence of numerous contaminants or the design of complex structures can often lead to delamination in carbon fiber composites. The main detection methods currently in use include ultrasonic testing, radiographic testing, eddy current testing and infrared thermography [7-11]. Among these, ultrasonic testing has become a mainstream technique for assessing the quality of CFRP structures due to its sensitivity to internal defects and its ability to achieve significant penetration depths [11]. However, traditional bulk-wave ultrasonic testing typically requires point-

by-point scanning, which is inefficient and unsuitable for rapid, large-area inspection [12]. As a type of guided wave, Lamb waves have significant applications in ultrasonic NDT. The Lamb wave technique has the outstanding advantages of strong penetration and minimal attenuation over long distances, and can be used to detect various defects, such as delamination, debonding and cracks [13-18]. Owing to these characteristics, Lamb wave technology has attracted considerable attention in the field of NDT of composite materials [19]. To localize defects in materials, actuators or sensors are usually positioned on the surface of CFRP laminates. Since Lamb waves scatter at the edges of defects when passing through them, comparing the signals from the defective plate with the baseline signals makes it possible to detect and localize defects in CFRP laminates. Most methods require prior knowledge of guided wave propagation within the structure, such as the modal characteristics of Lamb waves or time of flight (ToF). In contrast, the reconstruction algorithm for probabilistic inspection of damage (RAPID) does not require knowledge of guided wave propagation prior to imaging, and can swiftly and intuitively identify defect locations. It should be noted that the RAPID method also relies on baseline signals (i.e., reference signals from a healthy state), and the same applies to the method described in this paper. Velsor et al. [20] first proposed the RAPID algorithm, which is based on the damage index (DI). They successfully used this modified algorithm to monitor damage in pipelines. Subsequently, the RAPID was recognized as the fastest and most effective algorithm in the field of layered imaging, providing the best image quality. Sun et al. [21] proposed a probabilistic diagnostic imaging algorithm based on the Lamb wave delay factor. They calculated the ToF of the signal envelope by determining the group velocity of Lamb waves at a given frequency, and then compared this with the damage signal to construct a damage index. Meng et al. [22] measured ultrasonic response signals at various locations on the plate under different damage conditions. They used a constructed probability imaging algorithm to visualize the damaged areas. Experimental results showed that this method improved localization efficiency by excluding invalid sensor paths in the sensor network, reducing computational time by 31.32%. Chen et al. [23] used probabilistic imaging to estimate the range of defects, then recalculated the shape factor based on a given point along the path, and finally employed probabilistic superposition to locate the defects. The aforementioned methods require the complex sensor networks to be established and are limited in terms of imaging accuracy.

This requirement for specific parameters (e.g., frequency) makes defect detection more challenging in practical engineering applications and reduces the utility of such methods for NDT. To overcome these limitations, this paper proposes an improved defect identification approach that integrates an enhanced elliptical localization algorithm with Lamb wave probabilistic imaging. Although the proposed method employs a fixed sensor network, the number of sensors is significantly reduced compared to other methods. Both the excitation frequency and baseline signal are determined experimentally.

The main contributions are as follows: while maintaining the aforementioned engineering constraints (fixed sensor network, specific frequency, and baseline signals), we have significantly reduced the localization errors caused by CFRP anisotropy and improved the imaging focusing capability by introducing direction-dependent group velocity into the elliptical localization equation and combining it with signal differential coefficient (SDC)-weighted probabilistic imaging. Specifically, this methodology involves: (1) extracting key features (particularly ToF data) from Lamb wave signals to construct the elliptical localization paths, using direction-dependent group velocity $V(\theta)$ to compensate for CFRP anisotropy; (2) calculating the SDC by comparing defect and

reference signals to quantify signal deviation; and (3) developing an adaptive thresholding method based on local statistical characteristics to generate a probabilistic image of the defect region, enabling accurate delamination location.

To validate the proposed approach, the finite element models of CFRP containing controlled delamination defects are established, and an experimental setup incorporating ultrasonic excitation and FBGs sensing is constructed. The CFRP laminate specimens with and without pre-embedded delamination defects are designed and fabricated. The effectiveness of the proposed approach is systematically verified through simulations and experiments.

Because the proposed method requires a permanently attached sensor network, it is best suited for structural health monitoring (SHM) applications. For scenarios where fixed sensor installation is impractical, alternative NDT methods remain more appropriate. The specific engineering problem addressed is the rapid localization of manufacturing-induced delamination in CFRP laminates. The core challenges, such as anisotropy, modal coexistence and dense sensor requirements, are addressed via direction-dependent group velocity, symmetric excitation, and SDC-weighted multi-path fusion, enabling practical deployment as either a permanent SHM system or a rapid post-manufacturing inspection tool [24].

2 Principles and methods

2.1 General description of the detection principle

As illustrated in Fig. 1, the principle of the hybrid ultrasonic excitation-FBG sensing detection method can be described as follows: the pulse signals generated by the signal generator are amplified by a power amplifier and then applied to the piezoelectric wafer (PZT) attached to the CFRP surface. thereby exciting ultrasonic Lamb waves. Due to the dispersion characteristics of these waves, reflection, scattering and modal conversion phenomena occur when they encounter defects during propagation. The FBGs, which are arranged on the surface of the plate, serve as ultrasonic receivers that convert ultrasonics into light by detecting the local dynamic strain changes induced by the ultrasonics, which result in a center wavelength shift of the FBG reflection spectrum. An amplified spontaneous emission (ASE) broadband light source is used to illuminate the FBG sensor. The reflected light signals modulated by the Lamb waves, are first compensated by a reference grating, and then converted into an electrical signal by a high-speed photodetector. Finally, the signals are uploaded to the host computer via a data acquisition card. The signal processing algorithms are used to extract the characteristic parameters which are caused by defects, achieving defect localization and quantitative assessment. By combining the high sensitivity and electromagnetic interference resistance of FBGs with the multimodal coupling of Lamb waves, this method can significantly enhance the accuracy and robustness of CFRP detection.

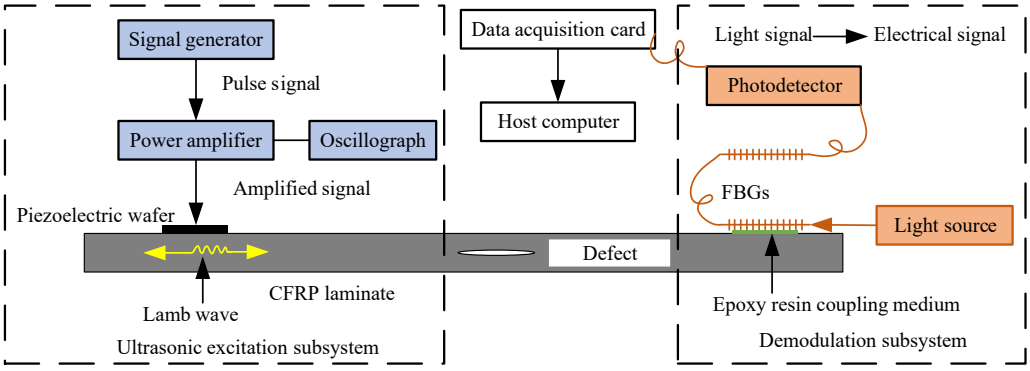

Fig. 1 Schematic of the principle of the hybrid ultrasonic excitation-FBG sensing detection method.

2.2 Defect identification approach integrating improved elliptical localization and Lamb wave probabilistic imaging

The principle of elliptical localization is described as follows: the excitation sensor and the receiving sensor are considered to be the two foci of an ellipse. The sum of the distances from the defect location to these two sensors is constant, i.e. the defect is located on the circumference of the ellipse [25], as illustrated in Fig. 2. This assumption is valid when the defect size is much smaller than the distance between the sensor and the defect, and when scattering is approximately isotropic [26, 27]. However, in practice, finite defect dimensions and material anisotropy introduce uncertainties [28, 29]. To mitigate these issues, the proposed method incorporates directional group velocity and probabilistic weighting. Assuming single scattering and a known ToF, and approximating the defect as an equivalent scattering center, a set of candidate scatter points satisfying a constant sum of propagation distances forms an elliptical trajectory. It is important to note that a single transmit-receive sensor pair can only define a region in which the defect may be located, rather than its exact position. The purpose of solving the elliptical equation is to generate candidate ellipses for multiple sensor paths. By superimposing these ellipses, the estimated defect location can be determined. In practice, real layered defects have finite dimensions, so the final imaging result reflects a region of high probability rather than a precise mathematical point. This multipath fusion strategy forms the basis for subsequent integration with the RAPID weighting scheme.

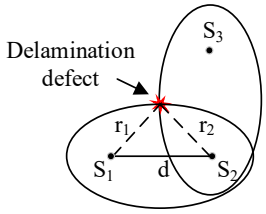

Fig. 2 Schematic of ellipse-based defect localization algorithm.

The core of the proposed defect localization strategy is to determine the defect coordinates (x, y) using multiple transmitter–receiver paths. As shown in Fig. 2, d is the distance between the excitation sensor S_i and a receiving sensor S_j. The constant sum of distances traces an ellipse with S_i and S_j as its foci. A single ellipse cannot uniquely determine the defect location, and it only provides a set of possible positions. However, by combining ellipses from multiple sensor pairs (e.g., S_1–S_2, S_1–S_3, etc.), their intersections or probabilistically weighted superposition converge to a high-probability region, yielding an estimated defect coordinate (x, y). To account for CFRP anisotropy,

the group velocity is refined using a direction-dependent wave speed $V(\theta)$. Additionally, the SDC from the RAPID framework is incorporated to weight the contribution of each sensing path. The semi-major axis of the ellipse a can be calculated using the following two equations:

$$r_1 + r_2 = ToF \cdot V(\theta) \tag{1}$$

$$a = \frac{1}{2} ToF \cdot V(\theta) \tag{2}$$

Let the coordinates of the two sensors be (x_1, y_1) and (x_2, y_2), respectively, then the focal length of the ellipse c can be expressed as follows:

$$c = \frac{\sqrt{|x_1 - x_2|^2 + |y_1 - y_2|^2}}{2} \tag{3}$$

This gives the semi-minor axis b of the ellipse:

$$b = \sqrt{a^2 - c^2} \tag{4}$$

The elliptical equation is then:

$$\frac{x^2}{a^2} + \frac{y^2}{b^2} = 1 \tag{5}$$

The anisotropy of CFRP laminates induces pronounced directional dependence in Lamb wave propagation characteristics, where the group velocity $V(\theta)$ varies obviously with the wave propagation angle θ relative to fiber orientation, resulting in significant localization errors in traditional defect localization algorithms. Therefore, introducing the directional group $V(\theta)$ enables the accurate calculation of the ToF of each propagation path, effectively resolving localization inaccuracies caused by material anisotropy.

The RAPID is a signal correlation-based method for defect detection and characterization. It employs a systematic comparison between reference signals and defect-induced signals to quantify perturbations in sensor path signal responses. By integrating these signal deviations with the spatial topology of sensor-actuator networks, RAPID can reconstruct a probabilistic distribution of the defect within the structural domain, enabling its precise localization and determination of its geometric shape. This algorithm involves two key computational modules: DI calculation and path image fusion reconstruction. The DI is a generalized measure used to quantify the degree of signal variation caused by defects along the Lamb wave propagation path. DI calculation is independent of any specific imaging framework; RAPID is merely one implementation method that utilizes DI for spatial probability mapping. In this paper, the degree of waveform distortion between the reference signal and the defect signal is defined as the DI, which is then used as the weighting criterion for subsequent probabilistic imaging. When Lamb waves encounter defect during propagation, their waveforms become significantly distorted, and the degree of distortion is proportional to the severity of the defect. The SDC is a mathematical measure of signal distortion, which can be expressed as [20]:

$$SDC = 1 - DI = 1 - \left| \frac{\int_{t_1}^{t_2} \left(S_{ref}(t) - \overline{S}_{ref} \right) \left(S_{def}(t) - \overline{S}_{def} \right) dt}{\sqrt{\int_{t_1}^{t_2} \left(S_{ref}(t) - \overline{S}_{ref} \right)^2 dt \cdot \int_{t_1}^{t_2} \left(S_{def}(t) - \overline{S}_{def} \right)^2 dt}} \right| \tag{6}$$

where $S_{ref}(t)$ is the baseline signal, $\overline{S}_{ref}$ is the mean value of $S_{ref}(t)$, $S_{def}(t)$ is the defect

signal, $\overline{S}_{def}$ is the mean value of $S_{def}(t)$, and t_1 and t_2 are the start and end moments of the intercepted signal, respectively. After obtaining the SDC values for all sensor paths, these values are mapped onto the structural domain to reconstruct the defect probability distribution. An elliptical distribution model is used to localize the SDC values spatially, with the geometry of the ellipse determined by the coordinates of two sensors. To improve the clarity of the spatial distribution of the SDC values and optimize the visualization of defect probability, a weight coefficient R is introduced for data normalization, which can be expressed as follows [20, 21]:

$$R(x,y)=\frac{1}{2}\begin{cases}\dfrac{\beta-d}{\beta-1}, 1\le d\le\beta\\ 0, d\ge\beta\end{cases} \tag{7}$$

$$d=\frac{\sqrt{\left(x_p-x\right)^2+\left(y_p-y\right)^2}+\sqrt{\left(x_s-x\right)^2+\left(y_s-y\right)^2}}{\sqrt{\left(x_p-x_s\right)^2+\left(y_p-y_s\right)^2}} \tag{8}$$

Eq. (8) defines the ratio of the sum of the distances from an arbitrary defect location (x, y) to the excitation transducer (x_p, y_p) and the receiver (x_s, y_s) relative to the sensor spacing. This ratio determines the elliptical geometry of the defect probability distribution, with the parameter β modulating the ellipse size. The data in Table 1 are based on the statistical averages of the simulation and experimental results presented in this paper. Image contrast is defined as the ratio of the maximum pixel intensity to the average intensity within the defect region. Under the test conditions, β=1.05 yields the smallest average localization error and the highest image contrast. It should be noted that the average localization errors reported in Table 1 are obtained from a simplified elliptical intersection model without the full probabilistic imaging pipeline. These values are used only for β optimization. Within the ellipse region of each sensor path, the defect probability follows a distinct gradient profile, decaying radially from the center to the boundary of the ellipse, where it asymptotically approaches zero.

Table 1 Localization error and image contrast for different β values (unit: mm)

β value	Center error-Defect (150, 150)	Center error-Defect (100, 100)	Average error	Image contrast
0.95	3.124	3.452	3.288	0.718
1.00	2.982	3.208	3.095	0.783
1.05	2.836	3.017	2.927	0.851
1.10	3.053	3.281	3.167	0.803
1.15	3.306	3.538	3.422	0.739

A single sensing path can only yield a localized defect probability distribution with its detection vicinity. To achieve precise defect localization in CFRP laminates, a distributed PZT-FBG sensing network must be deployed, enabling the integration of multi-path detection data. By performing image fusion and spatial superposition of the defect probability distributions derived from individual sensor paths, a comprehensive probabilistic assessment can be obtained. The resultant defect probability $P(x, y)$ at any coordinate (x, y) on the CFRP laminate can be mathematically expressed as follows:

$$P(x,y)=\sum_{k=1}^{N}SDC_k R_k(x,y) \tag{9}$$

where N represents the total number of sensing paths in the detection area and SDC_k represents the

SDC of the kth path.

From an implementation standpoint, the elliptical localization algorithm is a ToF-based defect localization method. Its accuracy is primarily limited by two critical factors: the precision with which the group velocity of Lamb waves is estimated, and the reliability with which scattered waves are extracted. In contrast, the RAPID algorithm offers superior localization accuracy, albeit with certain limitations. Firstly, it requires a densely distributed sensor network to ensure adequate spatial resolution. Secondly, its detection performance is highly sensitive to the geometric configuration of the sensor array, which could affect the robustness of the algorithm in practical scenarios.

Therefore, this paper proposes a improved approach to identifying defects in CFRP laminates by integrating an improved elliptical localization algorithm with Lamb wave probability imaging. This hybrid approach enables high-precision defect localization and high-resolution imaging, overcoming challenges such as material anisotropy, noise interference, and sparse sensor constraints. The flowchart is shown in Fig. 3.

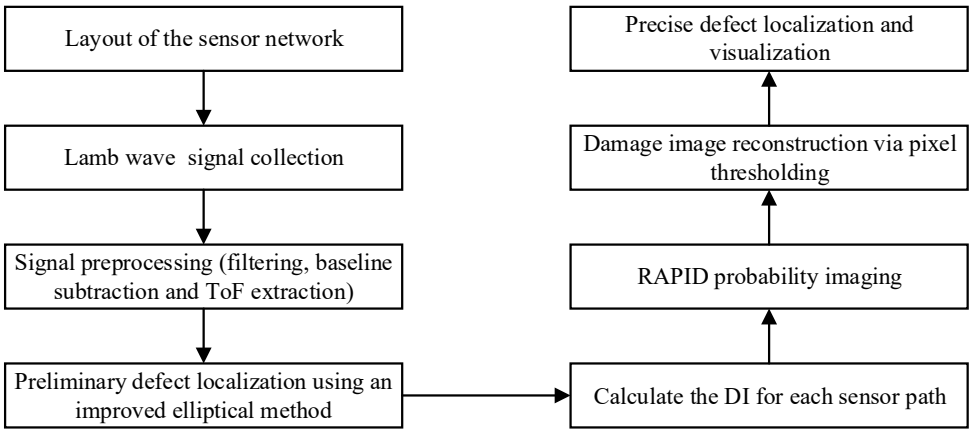

Fig. 3 Flowchart of the proposed approach for defect identification in CFRP laminates.

3 Finite element modelling and simulation for Lamb wave defect detection in CFRP laminates

3.1 Lamb wave frequency dispersion curves in CFRP laminates

The one-dimensional Gauss-Lobatto-Legendre semi-analytical finite element (1D-GLL-SAFE) method is primarily concerned with the solution of guided waves in isotropic and anisotropic materials. For anisotropic thin plates, the group velocity c_g has a radial component along the wavenumber k and a component perpendicular to the wavenumber k. Therefore, when the wavevector propagates at an angle θ with respect to the direction of the wavenumber, the two group velocity components in the Cartesian coordinate system can be calculated by [30]:

$$\begin{Bmatrix} c_{gx} \\ c_{gy} \end{Bmatrix} = \begin{bmatrix} \cos\theta & -\sin\theta \\ \sin\theta & \cos\theta \end{bmatrix} \begin{bmatrix} \dfrac{\partial\omega}{\partial k} \\ \dfrac{\partial\omega}{k\partial\theta} \end{bmatrix} \tag{10}$$

where the derivative $\frac{\partial\omega}{\partial\theta}$ can be approximated by the central difference method [30]:

$$\left.\frac{\partial \omega}{\partial \theta}\right|_{\theta=\theta_1} \approx \frac{\left.\omega(k)\right|_{\theta_1+\frac{\theta\Delta}{2}} - \left.\omega(k)\right|_{\theta_1+\frac{\theta\Delta}{2}}}{\Delta\theta} \tag{11}$$

Then the magnitude and direction of the group velocity in the anisotropic plate structure can be given by [30]:

$$\begin{cases} c_g = \sqrt{c_{gx}^2 + c_{gy}^2} \\ \theta_g = \arctan\left(\dfrac{c_{gy}}{c_{gx}}\right) \end{cases} \tag{12}$$

The CFRP laminate structure and the direction of Lamb wave propagation are shown in Fig. 4, with the propagation angle θ is rotated around the z-axis.

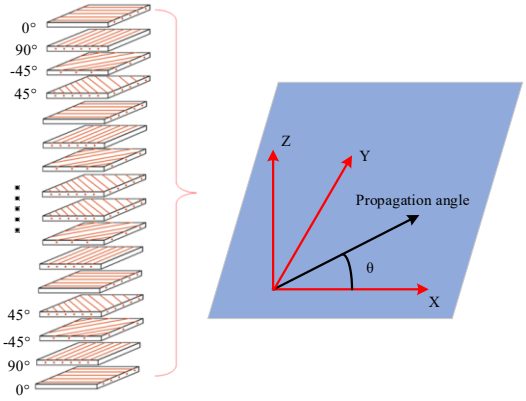

Fig. 4 Schematic representation of the CFRP laminate structure and the direction of Lamb wave propagation.

Dispersion curves of Lamb wave models (S_0 and A_0) propagating in a 16-layer CFRP laminate with a $[0/90/–45/45]_4$ layup are numerically generated using the SAFEDC software. The input parameters for dispersion curve calculation using SAFEDC are as follows: model thickness 2mm, in-plane dimensions 300mm×300mm, single-layer thickness 0.125mm (16 layers total), layup sequence $[0/90/-45/45]_4$, and the orthotropic elastic constants listed in Table 1. These parameters are converted into the stiffness matrix required by the semi-analytical finite element (SAFE) solver to obtain phase and group velocities. The wave propagation angle θ is varied from 0° to 180° in 5° increments to capture directional dependence, and the frequency range is set from 0 to 500 kHz with a step size of 1 kHz. Fig. 5 presents the radar maps of the phase and group velocities as functions of propagation direction. As shown in Fig. 5(a), the phase velocity of the S_0 mode ranges from 6110 to 6250m/s, while that of the A_0 mode varies between 1380 and 1450m/s. This significant variation reflects the pronounced anisotropy of the composite, with the A_0 mode exhibiting particularly strong velocity reduction at low frequencies. Correspondingly, as depicted in Fig. 5(b), the group velocity ranges from 6050 to 6170m/s for the S_0 mode and from 1250 to 1390m/s for the A_0 mode. The group velocity, which characterizes the energy propagation of Lamb waves, aligns with the variation trend observed in the phase velocity. Due to the inherent anisotropy of CFRP, Lamb wave velocities exhibit significant dependence on ply orientation and propagation direction. These directional variations provide critical information for subsequent defect localization and identification.

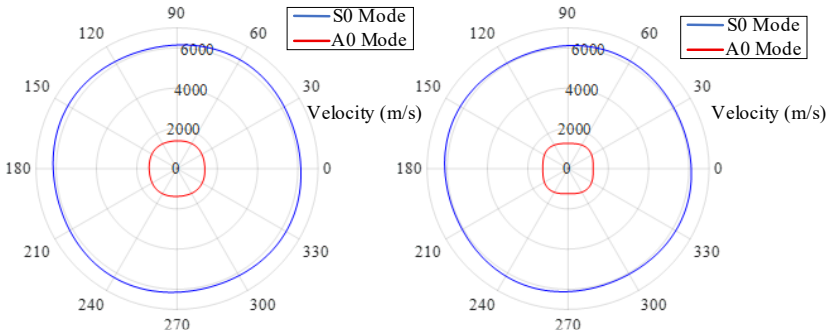

Fig. 5 Lamb wave modal velocity radar map in CFRP laminate: (a) phase velocity;(b) group velocity.

3.2 Finite element modelling

The 8-node linear brick element with reduced integration (C3D8R) is selected for the 3D solid modelling. This unit can withstand tensile, compressive, and shear stress loads, which correspond to the actual loading conditions experienced by the laminate during ultrasonic Lamb wave propagation. A structured meshing strategy is adopted to balance computational accuracy and efficiency. The in-plane element size is set to 0.5 mm, satisfying the widely accepted criterion of at least 10 elements per wavelength for the A0 mode at 200 kHz (wavelength approximately 8–10mm). In the thickness direction, each of the 16 plies is discretized using a single element, resulting in 16 elements through the thickness. The total number of elements is approximately 1440000 with 1540217 nodes. Mesh independence is confirmed by performing a mesh convergence check and comparing the results with those from a refined mesh with an in-plane size of 0.4mm; the ToF changed by less than 2%, and the localization error changed by less than 0.2mm. Thus, this meshing scheme ensures adequate resolution for Lamb wave propagation and defect scattering while maintaining a reasonable computational cost. In this paper, a CFRP laminate, T300/5028, is used for modelling and simulation analysis. The material parameters are given in Table 2: E_1, E_2 and E_3 denote the tensile moduli in the transverse, longitudinal and normal directions, respectively; G_{12} denotes the in-plane shear modulus; G_{13} and G_{23} denote the out-of-plane shear moduli; v_{11}, v_{13} and v_{23} denote the Poisson's ratios in each direction; ρ denotes the density of the material. Modelling is carried out using a $[0/90/-45/45]_4$ cyclic lay-ups. The fiber lay-up is shown in Fig. 6, and the local enlargement of the model is shown in Fig. 7.

Table 2 T300/5028 material parameters.

E_1 (GPa)	E_2 (GPa)	E_3 (GPa)	G_{12} (GPa)	G_{13} (GPa)	G_{23} (GPa)	v_{11}	v_{13}	v_{23}	ρ (kg/m^3)
132	10.5	10.5	5.65	3.38	5.65	0.24	0.59	0.24	1540

To ensure the accuracy of the solution and the reliability of the simulation results in the finite element meshing module, the minimum mesh size must be less than one-tenth of the Lamb wave wavelength. Based on calculations, the element size is set to 0.5mm. The distance between the piezoelectric wafer and the FBG is 200mm. The calculated propagation time of the A_0-mode Lamb wave in the scanning region is approximately 133μs, and the excitation signal duration is 25μs. Consequently, the total simulation duration is 158μs with a time step of 10μs.

The surface nodes of the complete laminate with its upper and lower layers are coupled during modelling, and are only distinguished from each other by the node codes [31], as shown in Fig. 8(a). The prefabrication of delamination defect is achieved by removing the coupled separation nodes from each other in the mode, as shown in Fig. 8(b).

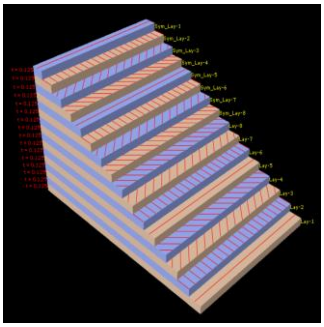

Fig. 6 Carbon fiber lay-up method.

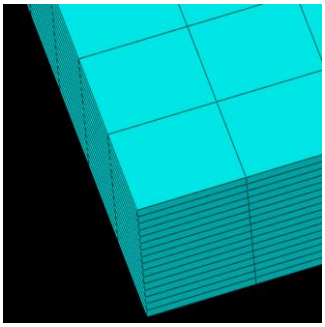

Fig. 7 Model local enlargement diagram.

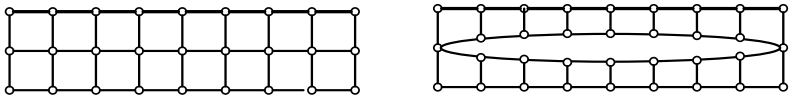

(a) (b)

Fig. 8 Schematic diagram of the nodes of the two layers of the laminate: (a) nodes not separated; (b) nodes separated.

3.3 Generation and loading of ultrasonic Lamb wave signals

The excitation frequency has a critical influence on modal composition, the wavelength relative to defect size, and the signal-to-noise ratio. At 200kHz with a laminate thickness of 2mm (frequency-thickness product of 0.4MHz×mm), both the S_0 and A_0 modes are present. The A_0 mode exhibits relatively stable group velocity, whereas the S_0 mode shows slightly higher dispersion. The wavelength at 200kHz is approximately 8–10mm for the A_0 mode, comparable to the 10 mm defect diameter and ensuring sufficient scattering interaction. Additionally, the PZT transducers and FBG sensors used in the experiments exhibit stable electromechanical coupling and optical response in the 150–250kHz range. In this paper, a five-cycle Hanning-window-modulated sinusoidal signal is selected as the excitation signal, which can be expressed by:

$$x(t)=\sin(2\pi ft)\cdot\left[0.5\left(1-\cos\left(\frac{2\pi ft}{5}\right)\right)\right] \tag{13}$$

where f is the center frequency of the signal. Fig. 9 gives its time and frequency domain waveforms with a center frequency of 200kHz. A longer burst improves frequency concentration but worsens arrival-time separation, whereas a shorter burst broadens the spectrum and aggravates modal overlap. The five-cycle Hanning-window-modulated sinusoidal signal strikes a good balance between time-domain resolution and spectral concentration, thereby minimizing spectral leakage and side lobes. While the S_0 and A_0 modes coexist at this frequency, the proposed method uses envelope-based ToF and SDC as joint indicators without strict modal separation, which remains a current limitation.

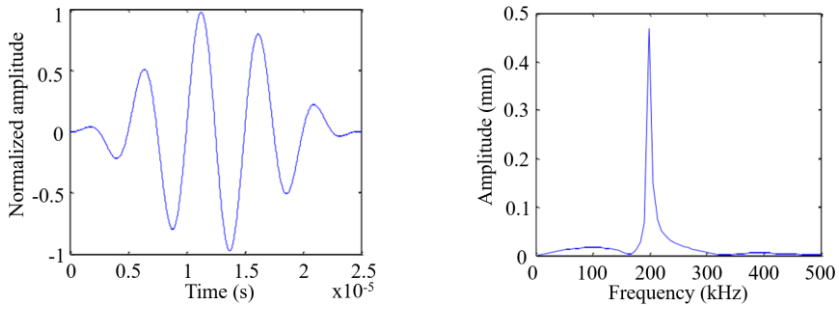

(a) (b)

Fig. 9 Sinusoidal signal modulated by five periods of a Hanning window: (a) time-domain; (b) frequency-domain.

In the loading module of the ABAQUS simulation software, the force load components in the x and y directions are set to 0, and the amplitude of the force load component in the z direction is set to 5 (i.e., CF1=0, CF2= 0 and CF3=5). Fig. 10 illustrates the sensor network layout and effective propagation paths in the CFRP laminate. As shown in Fig. 10(a), four elliptical intersectional regions indicate the range of delamination defect sites in the CFRP laminate. The precise location of defect can be identified by determining the intersection area of these ellipses. Fig. 10(b) presents the sensor network consisting of eight PZTs (S1 to S8). The green solid lines represent the effective propagation paths, whereas the dashed black lines denote the invalid paths. The PZTs are placed on both the top and lower bottom surfaces of the CFRP laminate. As the excitation signal waveform directly influences the Lamb wave mode, propagation characteristics and signal features, it must be designed appropriately. Since the A_0 mode primarily manifests as plate bending, synchronously pushing and pulling the upper and lower sensors enhances bending vibrations while suppressing the S_0 mode. This makes this configuration suitable for lower frequency ranges where the A_0 mode is more easily excited. The piezoelectric crystals are arranged symmetrically on the upper and lower surfaces of CFRP laminate, and in-phase pulse excitation signals (0° phase difference) are applied. Fig. 11 shows a schematic diagram of the excitation signal loading.

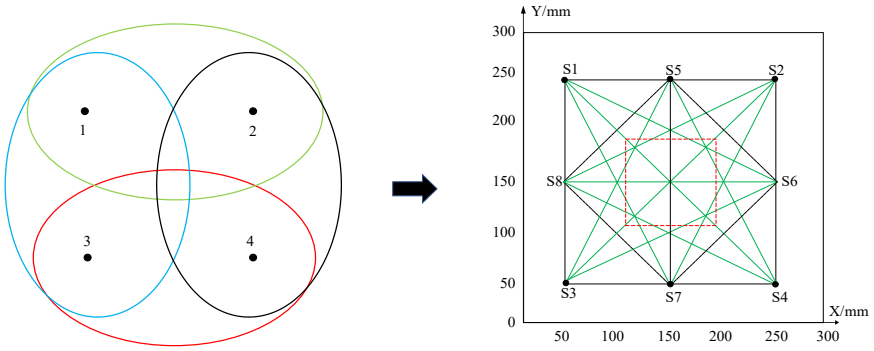

(a) (b)

Fig. 10 Schematic diagram of sensor network layout in the CFRP laminate: (a) defect probability distribution; (b) effective propagation path.

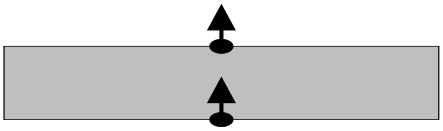

Fig.11 Schematic diagram of the excitation signal loading for Lamb wave generation.

Based on the adaptive thresholding method that uses local mean and standard deviation), the threshold for each pixel is dynamically determined from the statistics of its local window.

$$T(x,y) = \mu(x,y) + k \cdot \sigma(x,y) \tag{14}$$

where $T(x,y)$ is the adaptive threshold at pixel (x,y); $\mu(x,y)$ is the mean pixel value within the local window centered at (x,y); $\sigma(x,y)$ is the standard deviation within that window, reflecting the degree of dispersion of pixel values; k is the adjustment coefficient (typically 0<k<10), which controls the sensitivity of the threshold to the standard deviation. In regions with strong signals, the standard deviation is typically large, increasing the threshold to avoid misclassifying background noise. Conversely, in regions with weak signals, the standard deviation is small, lowering the threshold to suppress interference in low signal-to-noise ratio, resulting in a clearer final image and more accurate damage localization.

3.4 Simulation results and analysis

3.4.1 Propagation and signal acquisition of Lamb waves in CFRP laminates

Fig. 12 gives the propagation process of Lamb waves in the CFRP laminates, containing two cases: a defect-free plate and a laminate with a delamination defect. By comparing the propagation characteristics of the fluctuations in two cases, the propagation law of Lamb waves in anisotropic materials and the boundary reflection behavior interacting with the delamination defect can be clearly observed.

Fig. 12(a) and (b) show the propagation process of Lamb waves in a defect-free CFRP laminate, with an excitation source located at the center of the laminate. As can be observed in Fig. 12(b), at 130μs, the Lamb wave expands in all directions with an elliptical wavefront, which indicates that the anisotropic property of the CFRP laminate affects the wave speed, resulting in different speeds in different directions. The fluctuation at the excitation center is the most obvious and the shape of the wavefront gradually deforms as the wave propagates outwards due to the anisotropy of the laminate. When the Lamb wave propagates to the boundary of the laminate, an obvious wave reflection phenomenon occurs due to the boundary condition. Fig 12(c) and (d) illustrate the propagation process of Lamb waves in a CFRP laminate containing a delamination defect, with the excitation source shifted from the center of the laminate to the coordinates (50, 250). As can be seen, the Lamb wave propagates outwards from the excitation source with a relatively intact waveform until it approaches the defect area. However, local changes in material properties affect the wavefront morphology, indicating that the defect may modulate the wave velocity or amplitude. As shown in Fig. 12(d), at 120μs, the Lamb wave interacts with the delamination defect, resulting in significant waveform distortion. Some of the incident wave energy is reflected by the defect boundary (denoted by the red-marked region in the figure), while the rest passes beyond the defect with an altered waveform. In addition, distinct diffraction waves are generated at the defect edges, demonstrating the influence of structural inhomogeneity on wave propagation. This results in wave energy being redistributed along multiple propagation paths, highlighting the complex scattering mechanisms induced by the defect. By analyzing Lamb wave modifications and combining advanced signal processing methods, delamination defects can be accurately located and sized.

Fig. 13 shows the time-domain signals of Lamb waves propagating along three different paths: S1-S2, S1-S3, and S1-S4. As can be seen, the presence of a delamination defect markedly alters the propagation characteristics of Lamb waves. Compared to the reference signal from the defect-free laminate (red curve), the A_0 mode waveform acquired from the defective laminate (blue curve) exhibits obvious amplitude attenuation and phase delay as it passes through the defect area, indicating considerable energy loss due to the defect. The severity of this effect depends heavily on the propagation path. Pronounced waveform distortion is observed particularly along the 45°-oriented path S1-S4, highlighting the directional dependence of Lamb wave interaction with defects in anisotropic laminates. In addition, alterations in edge-reflected wave features demonstrate that the defect modifies the wave propagation path and energy distribution, thereby influencing the propagation behavior of Lamb waves.

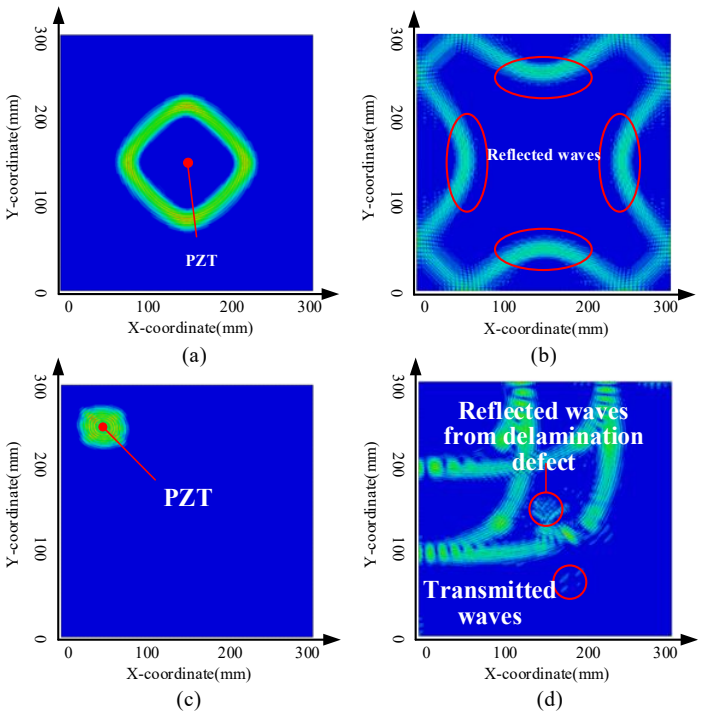

Fig. 12 Lamb wave course output cloud maps at different moments. (a) 60μs; (b) 130μs; (a) 30μs; (b) 120μs.

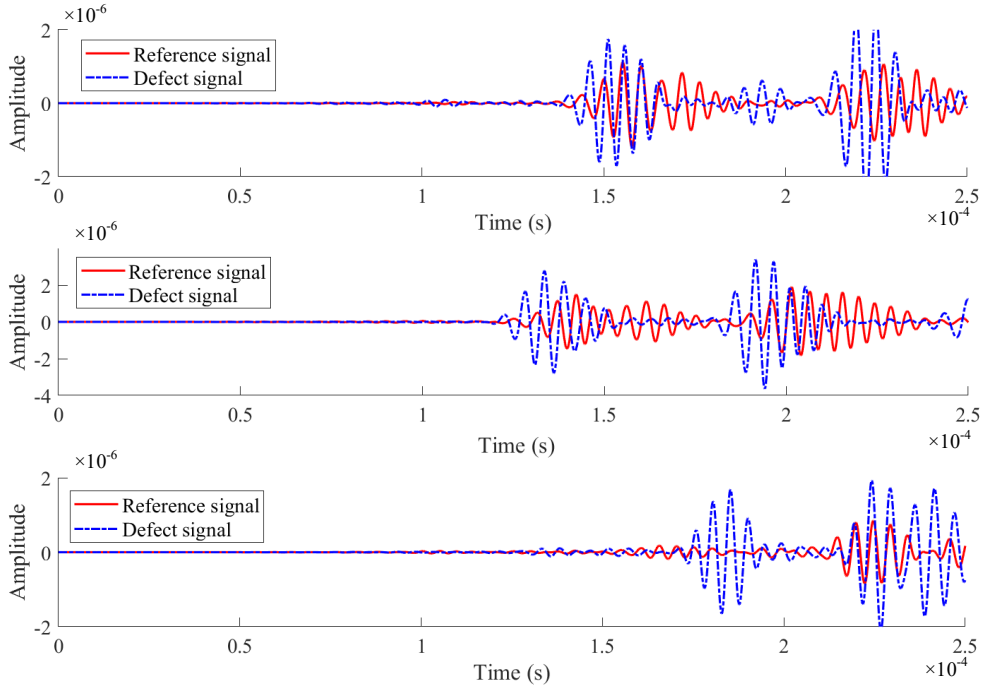

Fig. 13 Time-domain signals of Lamb waves acquired from three different paths: S1-S2, S3, S4.

3.4.2 Defect imaging and localization

The ToF and DI metrics are calculated using the corresponding path scattering signals and Eq. (6), as shown in Tables 3 and 4. To more intuitively verify the effectiveness of the proposed method, the reconstructed images of the defect region are generated. All probability plots are processed using the adaptive thresholding method described in Section 2.2, and no fixed global thresholds are used. The resulting defect probability distribution map and localization results are presented in Figs. 14 and 15. The specific locations of the delamination defects are indicated by white circles. In the

imaging results, the darker the color along a given propagation path, the higher the probability of defect at that location. The final defect location is determined as the intersection of the points with the highest pixel values from multiple paths. The ToF is influenced by the propagation time of the Lamb waves to the defect: The greater the distance between the defect the PZT, the longer the ToF. The center of the identified defect region (i.e., the grid point with the highest defect probability) is quantitatively assessed using the defect localization error, as summarized in Table 5.

Table 3 Simulation results (I): calculated values of ToF and DI.

Path	ToF (μs)	DI	Path	ToF (μs)	DI
S1-S4	165.6	0.6344	S3-S5	173.7	0.1971
S1-S6	151.5	0.1645	S3-S6	151.3	0.1550
S1-S7	166.4	0.1338	S4-S5	150.1	0.0093
S2-S3	168.3	0.4960	S4-S8	156.0	0.1600
S2-S7	170.1	0.0860	S5-S7	125.0	0.7301
S2-S8	149.3	0.0343	S6-S8	139.7	0.5993

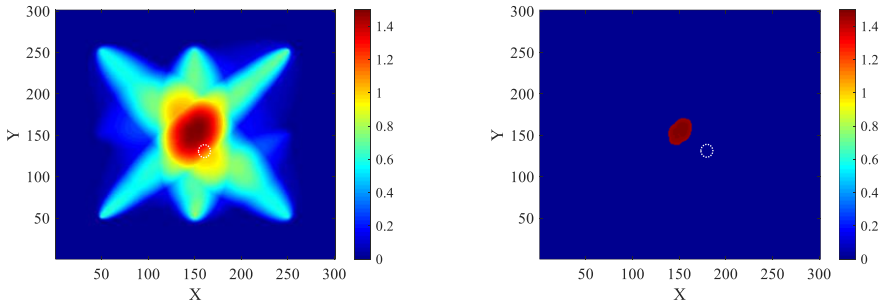

(a) (b)

Fig. 14 Simulation results (I): defect imaging and localization using the proposed algorithm: (a) defect image; (b) threshold-processed image.

Table 4 Simulation results (II): calculated values of ToF and DI.

Path	ToF (μs)	DI	Path	ToF (μs)	DI
S1-S4	168.2	0.1553	S3-S5	151.6	0.3960
S1-S6	170.8	0.0993	S3-S6	166.1	0.2550
S1-S7	149.9	0.7301	S4-S5	173.5	0.0093
S2-S3	165.7	0.8338	S4-S8	152.4	0.8600
S2-S7	151.2	0.1970	S5-S7	128.5	0.2301
S2-S8	156.8	0.0860	S6-S8	125.9	0.0993

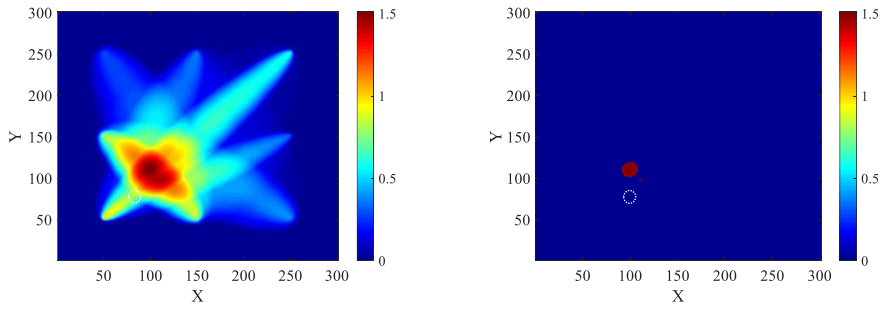

(a) (b)

Fig. 15 Simulation results (II): defect imaging and localization using the proposed algorithm: (a) defect image; (b) threshold-processed image.

Table 5 Defect localization error analysis for simulation results.

Defect position	Imaging position	Absolute error (mm)	Relative error (%)
(150.0, 150.0)	(153.0, 152.5)	3.91	1.85
(100.0, 100.0)	(102.4, 102.7)	3.61	2.55

4 Experimental verifications

4.1 Experimental setup

To validate the effectiveness of the proposed algorithm, an experimental setup is constructed according to the schematic illustrated in Fig. 1, with a physical photograph provided in Fig. 16. This setup employs the following instrumentation: a Tektronix AFG2021-SC signal generator, an NF Circuit Design HAS-4052 power amplifier, and a Tektronix MSO4034B digital oscilloscope. The PZTs made of lead zirconate titanate are employed for the excitation of Lamb waves. An amplified spontaneous emission (ASE) light source provides an output power of 14.33dBm over a wavelength range of 1520-1575nm. A reference grating is incorporated into the optical path to provide real-time compensation for power fluctuations of the ASE light source, thereby reducing environmental interference and improving measurement stability. Optical signals are detected using an FPD610 photodetector, which operates within the 950-1650nm wavelength range and offers a maximum stabilized responsivity of 1A/W. Data acquisition is performed via an 8-channel PCI Express data acquisition card, capable of sampling at rate up to 125MS/s.

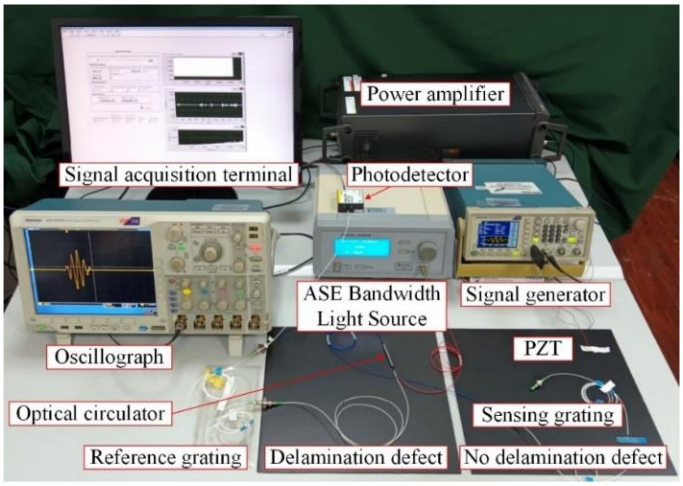

Fig. 16 Experimental setup.

4.2 Specimens and testing methods

Based on the finite element simulation models established in Section 3.2, three CFRP laminate specimens are designed and fabricated, as illustrated in Fig. 17. These specimens are manufactured through a hot-pressing molding process using 16 layers of prepreg (composed of carbon fiber-epoxy matrix with 70% fiber and 30% resin content by volume). Each layer has a nominal thickness of 0.125mm, resulting in a total laminate thickness of 2±0.05mm. The in-plane dimensions of each specimen are 300×300 mm². The plies are arranged in a specific order to form a symmetrical laminate. After the eighth ply, circular polytetrafluoroethylene (PTFE) films with a diameter of 10mm and a thickness of 0.025mm are placed at the pre-set defect center coordinates (150, 150) mm and (100, 100) mm, respectively. The remaining eight plies are then laid on top. A defect-free control specimen is fabricated using the same layering process but without the PTFE inserts. Fig.

17(a) presents the defect-free specimen, and Fig. 17(b) displays a specimen featuring a circular delamination defect with a diameter of 10mm, located at the center of the plate, as marked by the red circle. Fig. 17(c) shows another specimen (Sample C) containing a delamination defect identical in type and size to that in Fig. 17(b), but located in the lower-left region of the specimen at coordinates (100, 100) relative to the designed origin, as also marked with a red circle. As depicted in Fig. 18, the prefabricated delamination defects are all situated between the 8th and 9th layers of the laminate. To ensure long-term system stability, reference signals from the defect-free specimen are measured both before and after the experiments on the defective specimens. No significant drift is observed, confirming the repeatability of the experimental setup.

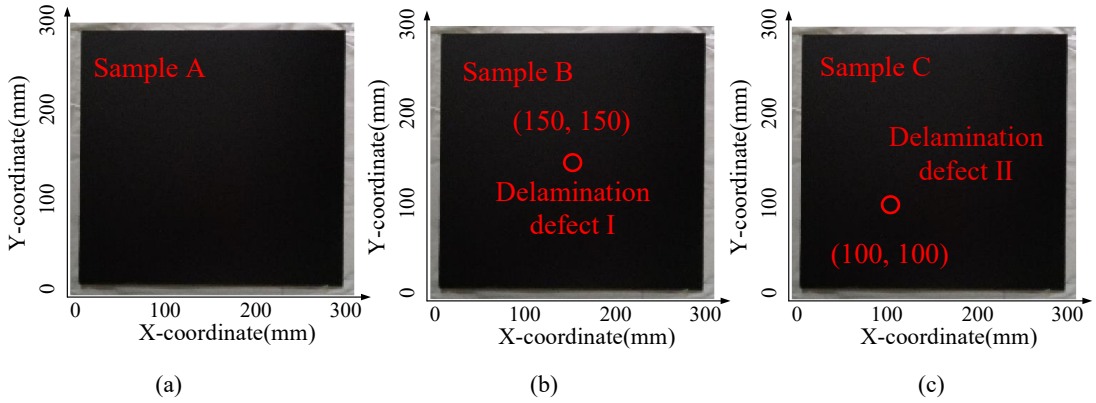

Fig. 17 CFRP laminate specimens: (a) the defect-free specimen; (b) the specimen with a delamination defect I; (c) the specimen with a delamination defect II.

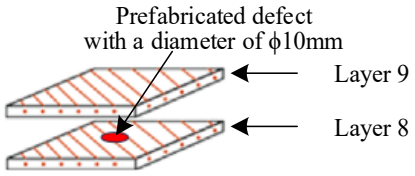

Fig. 18 Schematic diagram of a prefabricated delamination defect.

In this experiment, a single-shot multi-receiver strategy is adopted for defect detection in the CFRP laminates. As illustrated in Fig. 19, PZTs are used to excite Lamb wave signals at positions S1-S8, while FBG sensors are placed at the remaining positions to capture the response signals. The positions of all sensors are set to match those used in the simulation. The PZTs, which have a diameter of 10mm, are arranged symmetrically on both the top and bottom surfaces of the CFRP laminate in order to excite the A_0 mode of Lamb waves. Waveform signals are collected from twelve paths on both defect-free and defective specimens, yielding twelve sets of reference signals and twelve sets of signals from specimens with delamination, respectively. The scattered wave signals are subsequently obtained by calculating the signal difference between the reference and the defective waveforms for each corresponding path.

The proposed method primarily relies on ToF and waveform differences, which are quantified by the SDC. These parameters are less sensitive to amplitude changes than to variations in phase or waveform shape. Therefore, the current FBG configuration remains valid for method validation. However, because the orientation of the FBGs is fixed, the acquired signals represent only the dynamic strain components projected along the axial direction of each fiber, rather than the complete two-dimensional strain field. This directional sensitivity affects the comparability of amplitudes between different sensing paths, and limits the accuracy of amplitude-based defect quantification

and full-field imaging. Future work will explore multi-directional FBG arrays or hybrid PZT-FBG networks to reduce this dependency and achieve full strain field reconstruction.

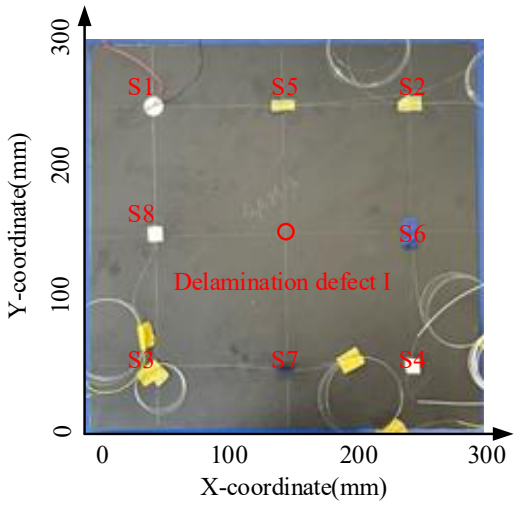

Fig. 19 Layout diagram of the sensor configuration used in the experiment.

4.3 Experimental signal acquisition and result analysis

To ensure the reliability of the experimental data, the following measures are implemented. First, for each sensing path, ultrasonic signals are acquired more than five times, and the average waveform is used for subsequent analysis to reduce random noise. Second, the experimentally measured ToF values are compared with the finite element simulation results for the same sensing paths; the deviation is consistently less than 5%, indirectly confirming the consistency of the experimental data. Fig. 20 gives the ultrasonic time-domain signals collected by the experimental setup for paths S1–S2, S1–S3 and S1–S4. As can be seen, the signal from the defective specimen (blue dashed line) differs significantly from the reference signal (red solid line) in amplitude, phase and waveform morphology. The overall reduction in signal amplitude indicates that the presence of defect causes energy scattering and attenuation during Lamb wave propagation, leading to a delayed arrival time of the wave packet at the FBG receiver compared to the reference case. These signal distortions are further influenced by high-frequency noise and background interference present in the experimental environment, which complicates direct extraction and interpretation of relevant wave features. To improve signal interpretability and defect-related feature visibility, the signal envelope is extracted using the Hilbert transform. The processed signals are illustrated in Fig. 21.

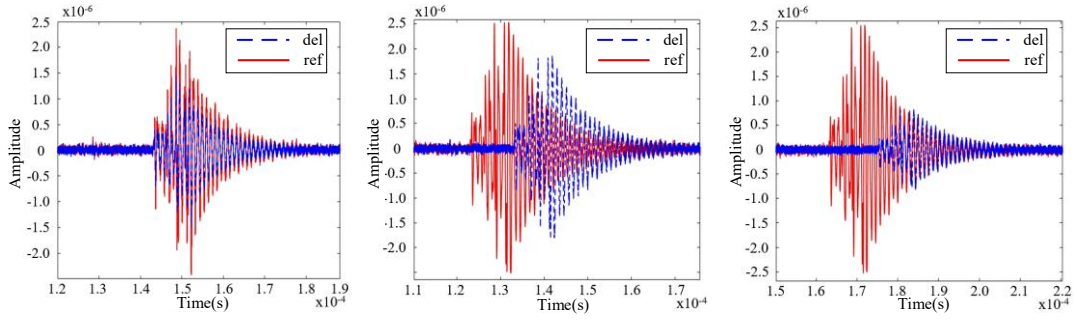

(a) (b) (c)

Fig.20 Experimentally collected ultrasonic time-domain signals for paths S1-S2, S1-S3 and S1-S4.

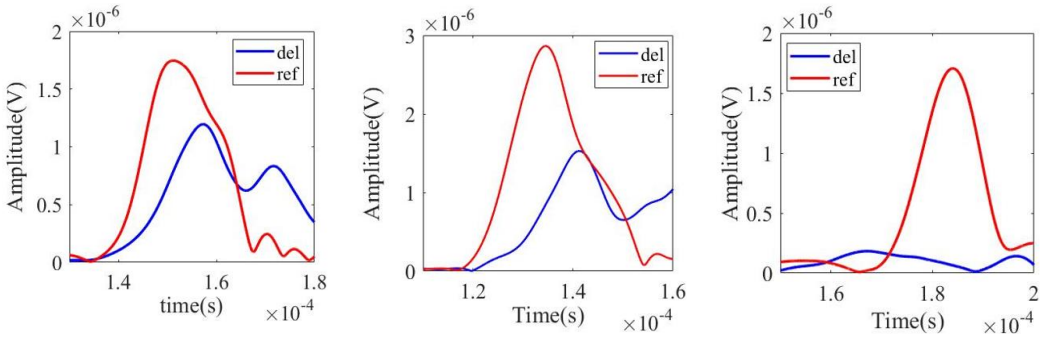

(a) (b) (c)

Fig. 21 Hilbert transform-derived signals corresponding to the processed ultrasonic responses from paths S1-S2 S1-S3 and S1-S4.

The ToF for both the reference and defective signals across all PZT excited-FBG receiver sensing paths is determined using the signal processing methodology in the simulation studies. The corresponding DI values are calculated using Eq. (6). The results are summarized in Tables 6 and 7. Defect reconstruction is conducted for each path, producing clear and accurate reconstructed images, as shown in Figs. 22 and 23. As can be observed, the pixel distribution of each sensing path is relatively concentrated, forming a region of high pixel density within the defect reconstruction image. By applying pixel thresholding to further process the initial reconstruction results, the defect regions are successfully isolated, resulting in the refined and accurate reconstructed images. The corresponding defect localization errors are provided in Table 8.

Table 6 Experimental results (I): calculated values of ToF and DI.

Path	ToF (μs)	DI	Path	ToF (μs)	DI
S1-S4	141.4	0.9001	S3-S5	171.0	0.2010
S1-S6	132.0	0.2110	S3-S6	162.9	0.1554
S1-S7	183.5	0.1033	S4-S5	154.0	0.1087
S2-S3	143.1	0.8400	S4-S8	172.0	0.2660
S2-S7	155.0	0.1290	S5-S7	143.9	0.8640
S2-S8	153.7	0.1870	S6-S8	162.8	0.7510

Table 7 Experimental results (II): calculated values of ToF and DI.

Path	ToF	DI (μs)	Path	ToF (μs)	DI
S1-S4	157.3	0.1238	S3-S5	168.6	0.5220
S1-S6	167.3	0.1022	S3-S6	160.7	0.2240
S1-S7	152.8	0.5830	S4-S5	164.3	0.0127
S2-S3	155.3	0.8020	S4-S8	171.2	0.6820
S2-S7	161,2	0.1532	S5-S7	167.0	0.4931
S2-S8	156.3	0.0933	S6-S8	162.9	0.0928

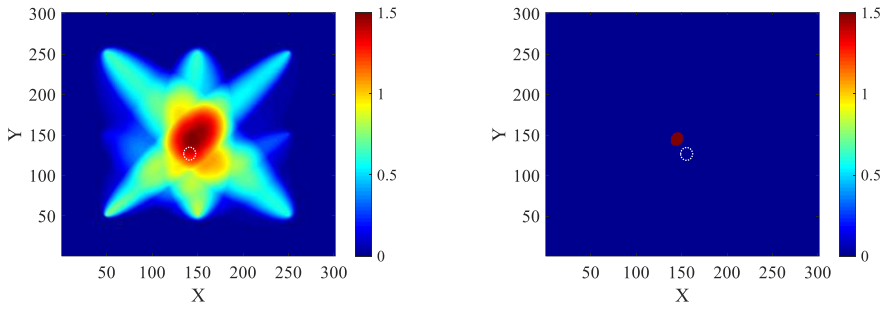

(a) (b)

Fig. 22 Experimental results (I): defect imaging and localization using the proposed algorithm: (a) defect image; (b) threshold-processed image.

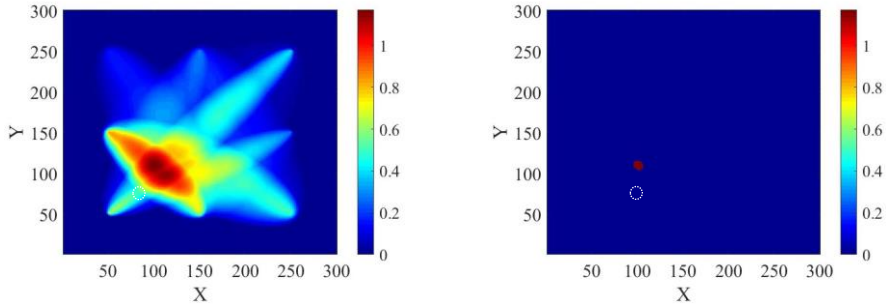

(a) (b)

Fig. 23 Experimental results (II): defect imaging and localization using the proposed algorithm: (a) defect image; (b) threshold-processed image.

Table 8 Defect localization error analysis for experimental results.

Defect position	Imaging position	Absolute error (mm)	Relative error (%)
(150.0，150.0)	(148.2, 147.8)	2.84	1.34
(100.0，100.0)	(102.5, 102.9)	3.82	2.71

5 Conclusions and future work

5.1 Conclusions

This paper proposes an improved defect identification approach that integrates an enhanced elliptical localization algorithm with Lamb wave probabilistic imaging to achieve high-precision delamination detection in CFRP laminates. The main contributions are summarized as follows:

(1) The dispersion curves of Lamb waves in the CFRP laminate are calculated using the 1D-GLL-SAFE method implemented in the SAFEDC software. Based on these results, the S_0/A_0 mode wave velocity radar map are generated to characterize their directional dependence within the composite structure.

(2) The finite element models of CFRP containing controlled delamination defects are established using the ABAQUS software to investigate the propagation characteristics of Lamb waves. The simulation results demonstrate that the proposed method achieves absolute errors of 3.91mm and 3.61mm, with corresponding relative errors of 1.85% and 2.55%, respectively.

(3) An experimental setup integrating ultrasonic excitation and FBG sensing is developed to validate the proposed defect detection method. CFRP laminate specimens, both with and without pre-embedded delamination defects, are designed and fabricated for testing. The experimental results show that this method achieves absolute errors of 2.84mm and 3.82mm, with corresponding

relative errors of 1.34% and 2.71%, respectively.

(4) This study provides a validated approach for NDT and localization of delamination defects in CFRP structures under laboratory conditions, supported by consistent simulation and experimental validation.

5.2 Limitations and future work

Despite the promising results, the following limitations remain:

(1) Fixed sensor network and baseline dependence. The proposed method requires permanently attached sensors and defect-free reference signals, limiting its use for one-time or in-service inspections. Future work will explore reconfigurable sensor arrays and self-referencing techniques (e.g., time-reversal).

(2) Uncalibrated wave velocity. The theoretical group velocity $V(\theta)$ has not been experimentally calibrated, and manufacturing deviations may introduce systematic ToF errors. Future work will conduct multi-angle laser ultrasonic calibration.

(3) Limited defect configurations and no size/contour analysis. Validation is performed for only two defect locations (10mm diameter, mid-plane depth). The proposed method focuses on centroid localization and does not provide reliable estimation of defect size or boundary contours. Future work will involve systematic parametric studies and full-wavefield imaging for size quantification.

(4) Modal overlap. At 200kHz, the A_0 and S_0 modes are not strictly separated. Although symmetric excitation suppresses the S_0 mode, boundary reflections may still cause interference. Future work will employ wavenumber filtering or time-frequency analysis.

(5) FBG directional sensitivity. The FBG only measures dynamic strain along the fiber axis, and its response to the amplitude of Lamb waves at different incident angles exhibits directional dependence. This effect is not compensated for in this study, which can affect the accuracy of the SDC path weights. Future work will use multi-directional FBG arrays (e.g., at 0°, 60° and 120°) or hybrid PZT-FBG networks to eliminate this dependence.

(6) Uncertainty quantification not performed. Experimental uncertainties (sensor positioning, noise and material variability) are not systematically quantified. Based on Refs. [32, 33], future work will integrate a deep learning-based uncertainty quantification framework (e.g., Flipout CNN) to provide confidence intervals for defect coordinates.

Funding

This work was supported by the National Natural Science Foundation of China [Grant No. 52175518].

Disclosure statement

No potential conflict of interest was reported by the author(s).

Data availability

Data underlying the results presented in this paper are not publicly available at this time but may be obtained from the authors upon reasonable request.

References

[1] Zhang J, Lin G, Vaidya U, et al. Past, present and future prospective of global carbon fiber composite developments and applications[J]. Composites Part B: Engineering, 2023, 250:

110463.
[2] Li N, Li Y, Jelonnek J, et al. A new process control method for microwave curing of carbon fiber reinforced composites in aerospace applications[J]. Composites Part B: Engineering, 2017, 122: 61-70.
[3] Das T K, Ghosh P and Das N C. Preparation, development, outcomes, and application versatility of carbon fiber-based polymer composites: a review[J]. Advanced Composites and Hybrid Materials, 2019, 2: 214-233.
[4] Hermansson F, Heimersson S, Janssen M, et al. Can carbon fiber composites have a lower environmental impact than fiberglass?[J]. Resources, Conservation and Recycling, 2022, 181: 106234-.
[5] Zimmermann N and Wang P H. A review of failure modes and fracture analysis of aircraft composite materials[J]. Engineering Failure Analysis, 2020, 115: 104692.
[6] Guo K, Liu X, Ren Y, et al. Experimental study on crashworthiness and failure mechanisms of aeronautical multi-fibers hybrid composite corrugated structures with Carbon, Glass, Kevlar[J]. Aerospace Science and Technology, 2023, 142(A): 108599.
[7] Xu X, Dai T, Luo J, et al. Detectability of delamination in laminated CFRPs with diverse stacking sequences using eddy current method with T-R pancake coil[J]. NDT & E International, 2023, 136: 102814.
[8] Gupta M, Khan M A, Butola R, et al. Advances in applications of Non-Destructive Testing (NDT): A review[J]. Advances in Materials and Processing Technologies, 2022, 8(2): 2286-2307.
[9] Han S, Li Q, Cui Z, et al. Non-destructive testing and structural health monitoring technologies for carbon fiber reinforced polymers: A review[J]. Nondestructive Testing and Evaluation, 2024, 39(4): 725-761.
[10] Wang B, He P, Kang Y, et al. Ultrasonic testing of carbon fiber-reinforced polymer composites[J]. Journal of Sensors, 2022, 2022(1): 5462237.
[11] Wang B, Zhong S, Lee T L, et al. Non-destructive testing and evaluation of composite materials/structures: A state-of-the-art review[J]. Advances in Mechanical Engineering, 2020, 12(4): 1687814020913761.
[12] Spytek J, Mrowka J, Pieczonka L, et al. Multi-resolution non-contact damage detection in complex-shaped composite laminates using ultrasound[J]. NDT & E International, 2020, 116: 102366.
[13] Hassani S, Dackermann U. A systematic review of advanced sensor technologies for non-destructive testing and structural health monitoring[J]. Sensors, 2023, 23(4): 2204.
[14] Chen J, Yu Z, Jin H. Nondestructive testing and evaluation techniques of defects in fiber-reinforced polymer composites: A review[J]. Frontiers in Materials, 2022, 9: 986645.
[15] Ramalho G M F, Lopes A M, da Silva L F M. Structural health monitoring of adhesive joints using Lamb waves: A review[J]. Structural Control and Health Monitoring, 2022, 29(1): e2849.
[16] He J, Guan X, Peng T, et al. A multi-feature integration method for fatigue crack detection and crack length estimation in riveted lap joints using Lamb waves[J]. Smart Materials and Structures, 2013, 22(10): 105007.
[17] He J, Huo H, Guan X, et al. A Lamb wave quantification model for inclined cracks with experimental validation[J]. Chinese Journal of Aeronautics, 2021, 34(2): 601-611.
[18] Rheinfurth M, Kosmann N, Sauer D, et al. Lamb waves for non-contact fatigue state evaluation

of composites under various mechanical loading conditions[J]. Composites Part A: Applied Science and Manufacturing, 2012, 43(8): 1203-1211.

[19] Su Z, Ye L, Lu Y. Guided Lamb waves for identification of damage in composite structures: A review[J]. Journal of Sound and Vibration, 2006, 295(3-5): 753-780.

[20] Velsor J K V, Gao H and Rose J L. Guided-wave tomographic imaging of defects in pipe using a probabilistic reconstruction algorithm[J]. Insight-Non-Destructive Testing and Condition Monitoring, 2007, 49(9): 532-537.

[21] Sun L, Wei J, Peng C, et al. Modified lamb wave delay factor-based multiply–sum probabilistic diagnostic imaging algorithm of composite structures[J]. IEEE Transactions on Instrumentation and Measurement, 2023, 72: 6004713.

[22] Meng L, Guo Z, Ma C. Research on multiple damage localisation based on fusion of the Lamb wave ellipse algorithm and RAPID algorithm[J]. Insight-Non-Destructive Testing and Condition Monitoring, 2024, 66(1): 34-40.

[23] Chen X and Hua T. Optimised shape factor for ultrasonic Lamb wave damage probability imaging[J]. Acoustics and Electronics Engineering, 2024(3): 48-53.

[24] Lu H, Haris M, Cantero-Chinchilla S, et al. Uncertainty-quantified unsupervised transfer learning for ultrasonic-based corrosion detection in underwater steel pipes[J]. Automation in Construction, 2025, 178: 106385.

[25] Huo H, He J and Guan X. A Bayesian fusion method for composite damage identification using Lamb wave[J]. Structural Health Monitoring, 2021, 20(5): 2337-59.

[26] Michaels J E. Detection, localization and characterization of damage in plates with an in situ array of spatially distributed ultrasonic sensors[J]. Smart Materials and Structures, 2008, 17(3): 035035.

[27] Flynn E B, Todd M D. A Bayesian approach to optimal sensor placement for structural health monitoring with application to active sensing[J]. Mechanical Systems and Signal Processing, 2010, 24(4): 891-903.

[28] Kudela P, Radzieński M, Ostachowicz W. Identification of cracks in thin-walled structures by means of wavenumber filtering[J]. Mechanical Systems and Signal Processing, 2015, 50: 456-466.

[29] Yue N, Aliabadi M H. Hierarchical approach for uncertainty quantification and reliability assessment of guided wave-based structural health monitoring[J]. Structural Health Monitoring, 2021, 20(5): 2274-2299.

[30] Liu M, Li L, Zhang Y, et al. Dispersion of guided waves in complex waveguides: a hybrid modeling technique combining Gauss-Lobatto-Legendre node collation and semi-analytical finite element method[J]. International Journal of Applied Mechanics, 2022, 14(08): 2250085.

[31] Sharma R, Mahajan P and Mittal R K. Fiber bundle push-out test and image-based finite element simulation for 3D carbon/carbon composites[J]. Carbon, 2012, 50(8): 2717-2725.

[32] Lu H, Zheng G, Hua Y, et al. Prediction of the Residual stiffness of composite materials under random vibration loading using a combined probabilistic random forest and probabilistic stiffness model[J]. ASCE-ASME Journal of Risk and Uncertainty in Engineering Systems, Part A: Civil Engineering, 2025, 11(2): 04025017.

[33] Lu H, Cantero-Chinchilla S, Yang X, et al. Deep learning uncertainty quantification for ultrasonic damage identification in composite structures[J]. Composite Structures, 2024, 338: 118087.